Directivity of a Planar Hard-Dielectric Fabry-Pérot Optical Ultrasound Sensor

Danny R. Ramasawmy*, Eleanor Martin, James A. Guggenheim, Benjamin T. Cox and Bradley E. Treeby
Department of Medical Physics and Biomedical Engineering, University College London, London, UK
*danny.ramasawmy.15@ucl.ac.uk

***Abstract*—A planar hard-dielectric Fabry-Pérot (FP) optical ultrasound sensor was modelled analytically to study how different wave modes affect the directionality. The sensor was modelled as a multilayered structure using the global matrix method. Modal dispersion curves were extracted from the model to enable features of the directional response to be linked to specific wave phenomena. The analytical model showed good agreement with the measured directional response. The key features of the directional response are linked to wave effects such as the water-substrate and water-spacer compressional and shear critical angles. A region of high sensitivity immediately after the shear critical angle is associated with a leaky-Rayleigh wave which has a frequency-dependent phase speed. At higher frequencies, this region is diminished by a minimum which occurs when the mirrors have the same vertical displacement, resulting in a lack of sensitivity.**

***Index Terms*—Fabry-Pérot, directivity, non-specular reflection, matrix methods**

I. Introduction

The Fabry-Pérot (FP) optical sensor can detect ultrasound with high sensitivity over a broadband frequency range (tens of MHz), with small element sizes (tens of microns). It is frequently used in photoacoustic imaging and can be used for general ultrasound field characterization [1]. However, the ultrasound field measurements are affected by a complex directional response caused by the multilayered structure of the FP sensor. A model of the sensor directivity, and in particular of how it relates to the specific wave types in the sensor, will not only inform future sensor design, but could be used to deconvolve the directional response from array measurements made with the sensor. The use of an analytical model for the deconvolution avoids the difficulties presented by the noise inherent in an experimentally measured directional response [2], [3].

In this paper, a robust hard-dielectric FP sensor is analyzed [3]. This sensor is suitable for measurement of high acoustic pressures as found, for example, in high-intensity focused ultrasound (HIFU) [4]. The multilayered structure of the FP sensor consists of two partially reflecting dielectric mirrors separated by a thin spacer deposited on a substrate, as shown in Fig. 1. The sensor mirrors are constructed from six sets of alternating layers of silicon dioxide, SiO_2, and zirconium dioxide, ZrO_2, separated by a spacer made from SiO_2. The properties of the sensor materials can be found in Table I. A focused scanning laser beam at the base of the substrate is multiply reflected by the mirrors and the reflected light intensity is measured. An incident ultrasound wave modulates the distance between the mirrors changing the path length of the laser and hence the intensity of the reflected light.

A model of the normal incidence frequency response given by Beard et al [5], was extended by Cox & Beard [6], to model the FP frequency-dependent directivity of a thin-film polymer sensor up to 15 MHz. This three-layer analytical model is only applicable to sensors for which the mirror thickness is negligible, which is not the case here. Here, this work is extended to an arbitrary number of visco-elastic layers thereby allowing mirrors of finite thickness to be included. The model is then used to explain the directional response in terms of wave modes.

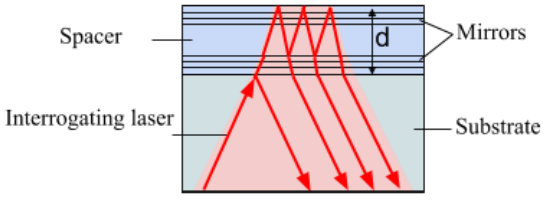

Fig. 1. Schematic of the Fabry-Pérot interferometer. Two dielectric mirrors separated by a SiO_2 spacer, with total thickness d, are deposited onto a glass substrate. The sensor is scanned by a focused laser beam at the base of the substrate. The beam is multiply reflected between the mirrors and the reflected intensity measured.

II. Model of Frequency-Dependent Directionality

A. Transduction Mechanism and Directivity

With reference to Fig. 1, the light from the interrogating laser beam is multiply reflected from both mirrors. The intensity from the superposition of the multiply-reflected light wave-fields is measured. The phase difference between the two points of reflection is $\phi = 4\pi nd/\lambda_0$, where n is the refractive index, d is the distance between the mirrors, and λ_0 is the wavelength of the interrogating laser light. In the presence of an acoustic wave, the change in intensity of the reflected beam resulting from a change in phase may arise from two mechanisms. The first is a thickness change as the distance between the mirrors is modulated when an acoustic wave passes through, and the second is from a change in the refractive index of the spacer. In many cases, the latter mechanism has been found to be negligible, and is

This work was supported by the EPSRC-funded UCL Centre for Doctoral Training in Medical Imaging (EP/L016478/1) and the Department of Healths NIHR-funded Biomedical Research Centre at NIHR Biomedical Research Centre at University College London Hospitals.

TABLE I
TABLE OF MATERIAL PROPERTIES

Material	$c_L(ms^{-1})$	$c_S(ms^{-1})$	$\rho(kgm^{-3})$
Water	1448	0	1000
Glass	5600	3500	2500
SiO_2	5900	3300	2500
ZrO_2	3000	1500	5680
Av.HD*	4953	2488	3988

*Average mirror properties weighted by thickness.

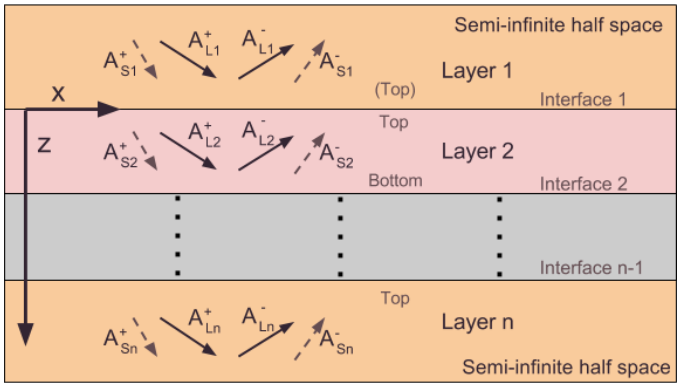

Fig. 2. Labelling notation for the GMM for a system of n-elastic layers, there are four bulk waves in each layer consisting of compressional (L, solid) and shear (S, dotted) waves travelling upwards (-) or downwards (+). The sum of one bulk wave type in a single layer is given by a complex amplitude A. The stress and displacement, from the bottom and top of the interface of adjacent layers, must be continuous.

not considered here [6]. The change in phase, $\Delta\phi$, from the modulation of the spacer thickness due to an external acoustic pressure change, Δp, can be written as

$$\Delta\phi = \left(\frac{4\pi n}{\lambda_0}\right)\frac{\partial d}{\partial p}\Delta p. \tag{1}$$

The term $\partial d/\partial p$ gives the sensitivity of the thickness to an external acoustic pressure change. The change in thickness is given by the difference in vertical displacement, u_z, from the initial distance, d, between the two mirrors. Hence the sensitivity of thickness to a pressure change is

$$\frac{\partial d}{\partial p} = \frac{u_z(d) - u_z(0) - d}{\Delta p}. \tag{2}$$

For an incident pressure wave of unit amplitude, $\Delta p = 1$, and $\partial d/\partial p$ is simply the change in thickness.

The frequency-dependent directional response can be calculated by averaging $\partial d/\partial p$ over the area illuminated by the focused laser beam, weighted by the beam profile $S(x)$:

$$D(f,\theta) = \frac{\int_{-\infty}^{\infty}(\partial d/\partial p)S(x)dx}{\int_{-\infty}^{\infty}S(x)dx}. \tag{3}$$

An example of this calculation when weighted by a top-hat laser beam profile can be found in [6] and a more detailed explanation of the FP transduction mechanism can be found in [5].

B. Global Matrix Method

The global matrix method (GMM) describes elastic and visco-elastic wave propagation in multilayered media [7], allowing all 30 layers in the hard-dielectric FP sensor to be modelled. As mentioned in Section II-A, the vertical displacement at each mirror is needed to calculate directivity. The well known isotropic stress-strain relationship for elastic materials and strain tensor for small deformations [7], can be combined to give the time-varying vector particle displacement

$$\rho_0\frac{\partial^2\mathbf{u}}{\partial t^2} = (\lambda+2\mu)\nabla(\nabla\cdot\mathbf{u}) - \mu\nabla\times(\nabla\times\mathbf{u}). \tag{4}$$

Using the Helmholtz method [8], the displacement vector can be written as $\mathbf{u} = \nabla\phi + \nabla\times\boldsymbol{\psi}$, and Eq. (4) can be written as two separate wave equations:

$$\frac{\partial^2\phi}{\partial t^2} - c_L^2\nabla^2\phi = 0, \tag{5}$$

$$\frac{\partial^2\boldsymbol{\psi}}{\partial t^2} - c_S^2\nabla^2\boldsymbol{\psi} = 0, \tag{6}$$

where ϕ and $\boldsymbol{\psi}$ are scalar and vector potentials. Equation (5) describes compressional waves based on the scalar potential and Eq. (6) describes shear waves where $\boldsymbol{\psi}$ points perpendicular to the displacement $\nabla\times\boldsymbol{\psi}$ and the direction the wave travels. The model is simplified to two dimensions (2D) by defining the vector potential as $\boldsymbol{\psi} = (0,\psi,0)$, where ψ is a scalar [6]. This constrains the shear wave propagation to be only vertically polarized in the plane (x,z), thus excluding the out-of-plane motion of horizontally polarized shear waves and Love modes. This is not a limitation as, by definition, horizontally polarized shear waves will not affect the vertical displacement of the sensor, which is needed to calculate the directional response. The resulting displacement vector is

$$\mathbf{u} = \left(\frac{\partial\phi}{\partial x} - \frac{\partial\psi}{\partial z}, 0, \frac{\partial\phi}{\partial z} + \frac{\partial\psi}{\partial x}\right). \tag{7}$$

Plane wave solutions to Eq. (5) and Eq. (6), at a single frequency, take the form $\phi = A_L\exp\{i(\mathbf{k}\cdot\mathbf{x}-\omega t)\}$ and $\psi = A_S\exp\{i(\mathbf{k_t}\cdot\mathbf{x}-\omega t)\}$, where A_L and A_S are the compressional and shear wave amplitudes, $\mathbf{k}$ is the wavenumber vector, and ω is the circular frequency. The stress and displacement within each layer of the FP sensor can be found from the superposition of acoustic fields from four bulk waves. These are upward and downward travelling longitudinal and shear waves and can described by a complex amplitude, as shown in Fig. 2.

The simplified 2D model results in four boundary conditions at the interface between two adjacent elastic layers. For perfectly bonded elastic layers, the normal, σ_{zz}, and shear, σ_{xz}, stress, and normal, u_z, and transverse, u_x, displacement must be continuous across the interface [7]. Therefore there are four equations for every interface in the system. At a solid-liquid interface there exists only three boundary conditions as there is no continuity of transverse displacement.

The equations for an n-layered structure can be assembled into a single (global) matrix which consists of $4(n-1)$ equations and $4n$ unknown wave amplitudes [7]. Knowledge of

four of the wave amplitudes allows the system to be rearranged and solved for the remaining amplitudes. Since water can only support a compressional wave and there are no waves travelling in the negative z-direction of the substrate backing, three of the wave amplitudes in the half-spaces ($A^+_{S1}, A^-_{Ln}, A^-_{Sn}$ in Fig. 2) are set to zero. Additionally the wave amplitude for the incident compressional wave in water, A^+_{L1}, can be set to 1 with no loss of generality. The complex reflection coefficient is calculated by taking the ratio of the reflected wave amplitude and incident wave amplitude, $R = A^-_{L1}/A^+_{L1}$. In addition, the dispersion curves for the sensor model can be obtained by finding the frequency-wavenumber pairs at which the determinant of the global system matrix is singular. Evaluating the GMM with a complex wavenumber allows absorption to be added to individual layers. Additionally, a small imaginary part of the wavenumber allows the leaky-Rayleigh wave to be easily identified [9].

III. Directivity Analysis

A. Experimental Directivity Measurements

The model was compared to directivity measurements of the planar hard-dielectric sensor presented in [3]. To record these measurements, the FP sensor was mounted within the base of a specially designed water bath suspended above the optics needed for the interrogation of the sensor. A broadband (up to 50 MHz) plane wave photoacoustic source attached to a rotating stage was incremented at $0.25°$ intervals about the point of interrogation on the surface of the FP sensor. A focused laser beam, tuneable in the range of $1440 - 1640$ nm (Tunics T100S-HP, Yenista Optics, France), was used to measure the FP sensor at an acquisition rate of 200 Hz. The measured time series were Fourier transformed to give the frequency-dependent directional response of the FP sensor. A more detailed description of the directivity measurement can be found in [10].

B. Feature Analysis

The analytical model shows good agreement with the measured directional response as shown in Fig. 3, where the key features have been labelled. In order to gain a greater understanding of the origin of the features in the directional response, Fig. 4(a)-(c) shows plots of the magnitude of the complex reflection coefficient, $|R|$ (solid line), and the normalized directivity (dashed) of Fig. 3(b) at three frequencies.

The first critical angle, θ_{c_L}, can be identified in Fig. 4(a)-(c) as the peak in $|R|$ at 15°. This peak is linked with a sharp dip in directivity. At the lowest frequency shown (0.1 MHz) the critical angle peak is sharp but broadens as the frequency increases. This is due to the increasing significance of the thin layers at the shorter wavelengths, so the reflected energy is spread over a wider angular range between the water-substrate and water-spacer critical angles. At very high frequencies, beyond those displayed, this peak becomes a double cusp, peaking at both critical angles. At angles just above after the compressional critical angles, $|R|$ dips and deepens as the frequency increases (> 35 MHz), causing a small peak in

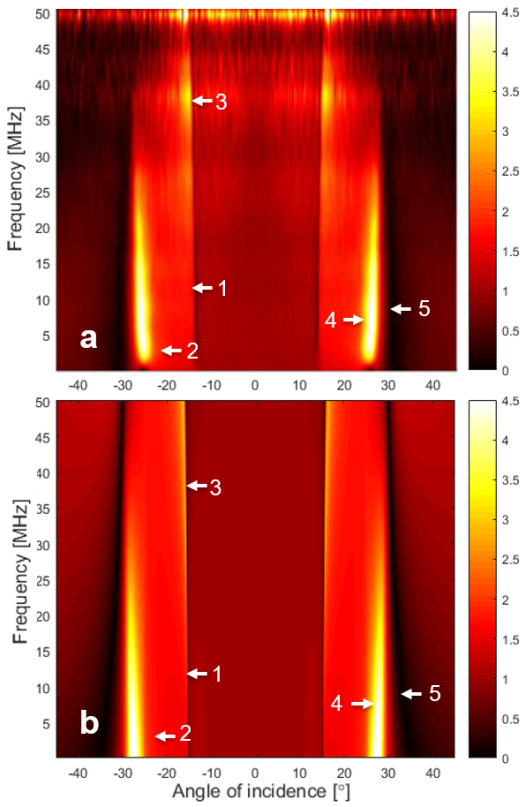

Fig. 3. Directivity measurement (a) and model (b) of the Fabry-Pérot interferometer. Key features which are common to both: 1 & 2) compressional and shear critical angles, 3) peak after water-substrate and water-spacer compressional critical angles at high frequencies, 4) peak preceding Rayleigh wave with a frequency-dependent phase speed, 5) minimum from no difference in the vertical displacement of the mirrors.

directivity which can be seen in Fig. 3(a)-(b) label (3). There is a small discontinuity in the directional response, seen in Fig. 4(a)-(c), associated with the water-substrate shear critical angle, θ_{C_S}, at 25°.

The maximum peak in the directivity occurs immediately preceding the leaky-Rayleigh wave angle, θ_R, which can be identified by a characteristic dip in $|R|$, seen in Fig. 4(a)-(c) and Fig. 3 label (4). At low frequencies, the phase speed of the Rayleigh wave is that of a Rayleigh wave travelling on the water-substrate interface ($0.91c_{S,\text{glass}}$). As the frequency increases, the effect of the mirrors and substrate becomes significant, and the Rayleigh phase speed moves towards the average shear speed of the mirrors and spacer, seen in Fig. 4(e)-(f). At even higher frequencies (not shown here), higher order Rayleigh modes will appear [9], [11].

The directivity peak associated with the leaky-Rayleigh wave is diminished by the crossing of the minimum highlighted in Fig. 4(c)-(d). This moves from a higher to a lower angle as the frequency increases from $0.1 - 50$ MHz. This minimum is a not a feature of the GMM, but a result of the transduction mechanism. The minima occur where the two vertical displacements in Eq. (2) are identical. Hence, there is no difference in vertical displacement and the interferometer is not sensitive to a change in pressure from an acoustic wave.

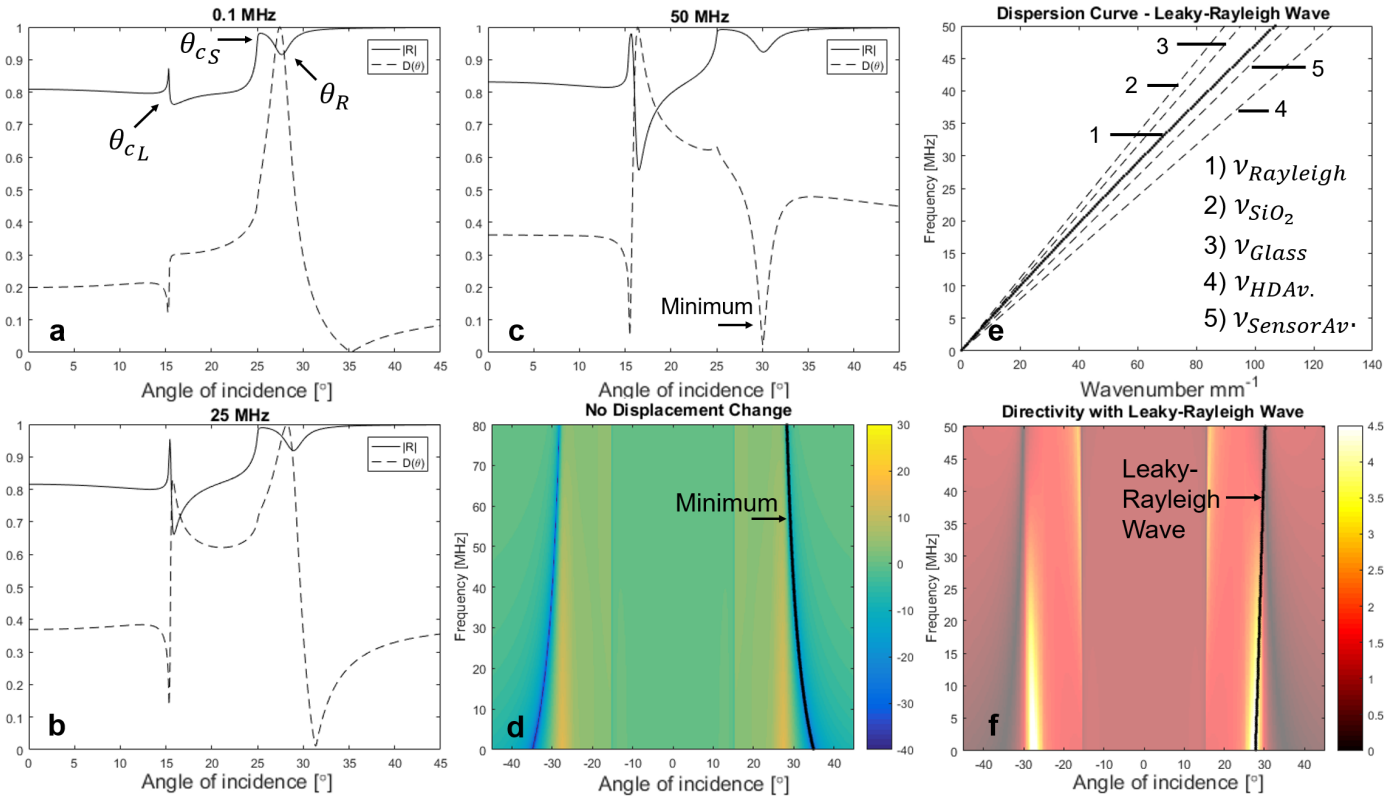

Fig. 4. (a)-(c) Magnitude of the normalized directivity (dashed line) and reflection coefficient (solid line), evaluated with an imaginary wavenumber component at different angles. The first (θ_{C_L}) and second (θ_{C_L}) critical angles produce a dip and peak in the directivity. Immediately after the first critical angle, there is a peak in directivity. The Rayleigh angle (θ_{C_R}) moves as the leaky-Rayleigh wave phase speed changes from 91% shear speed of the glass substrate to the average shear speed in the mirrors and spacer, as can be seen in (e)-(f). The minimum seen in (d), which has been plotted in dB scale for clarity, cuts across the Rayleigh wave and is caused when the vertical displacement is identical at the two points of reflection from the laser beam.

IV. Summary

The main aim of this paper was to investigate how different wave modes affect the directionality of a hard-dielectric FP ultrasound sensor. An analytical model based on the GMM showed good agreement when compared with measured directivity data. Using the GMM model, the main features in the directional response, shown in Fig. 3, were linked with different physical wave phenomena. In future, the model could be used to help deconvolve the directional response for array measurements made with a hard-dielectric FP sensor.

Acknowledgment

The authors thank Paul Beard for useful insights and discussions.

References

[1] E. Zhang, J. Laufer, and P. Beard, "Backward-mode multiwavelength photoacoustic scanner using a planar Fabry-Perot polymer film ultrasound sensor for high-resolution three-dimensional imaging of biological tissues," *Appl. Optics*, vol. 47, no. 4, pp. 561–577, 2008.

[2] A. M. Hurrell and S. Rajagopal, "The practicalities of obtaining and using hydrophone calibration data to derive pressure waveforms," *IEEE Trans. Ultrason., Ferroelect., Freq. Contr.*, vol. 64, no. 1, pp. 126–140, 2017.

[3] E. Martin, E. Z. Zhang, J. A. Guggenheim, P. C. Beard, and B. E. Treeby, "Rapid spatial mapping of high intensity focused ultrasound fields using a planar Fabry-Perot sensor," *IEEE Trans. Ultrason., Ferroelect., Freq. Contr.*, Under Review.

[4] E. Martin, E. Z. Zhang, P. C. Beard, and B. E. Treeby, "Rapid spatial mapping of the acoustic pressure in high intensity focused ultrasound fields at clinical intensities using a novel planar Fabry-Perot interferometer," in *IEEE Int. Ultrason. Symp.*, 2015.

[5] P. C. Beard, F. Perennes, and T. N. Mills, "Transduction mechanisms of the Fabry-Perot polymer film sensing concept for wideband ultrasound detection," *IEEE Trans. Ultrason., Ferroelect., Freq. Contr.*, vol. 46, no. 6, pp. 1575–1582, 1999.

[6] B. T. Cox and P. C. Beard, "The frequency-dependent directivity of a planar Fabry-Perot polymer film ultrasound sensor," *IEEE Trans. Ultrason., Ferroelect., Freq. Contr.*, vol. 54, no. 2, 2007.

[7] M. Lowe, "Matrix techniques for modeling ultrasonic waves in multilayered media," *IEEE Trans. Ultrason., Ferroelect., Freq. Contr.*, vol. 42, pp. 525–542, jul 1995.

[8] J. L. Rose, *Ultrasonic Waves in Solid Media*, vol. 107. Cambridge University Press, 2004.

[9] D. B. Bogy and S. M. Gracewski, "On the plane wave reflection coefficient and nonspecular reflection of bounded beams for layered half spaces underwater," *J. Acoust. Soc. Am.*, vol. 74, no. 2, pp. 591–599, 1983.

[10] J. A. Guggenheim, J. Li, E. Z. Zhang, and P. C. Beard, "Frequency response and directivity of highly sensitive optical microresonator detectors for photoacoustic imaging," Proc. SPIE 9323, 93231C, 2015.

[11] G. Farnell and E. Adler, "Elastic wave propagation in thin layers," in *Physical Acoustics* (W. P. Mason and R. N. Thurston, eds.), ch. 2, pp. 35–127, Academic Press, 2012.